第 50 卷 第 9 期/2023 年 5 月/中国激光 研究论文

中国激光

面向临床手术的激光钻切骨孔微观组织及抗失稳行为

陈梦雪[1,2,3]，季凌飞[1,2,3*]，张犁天[1,2,3]，曹丽杰[1,2,3]，韦杭汝[1,2,3]，孙伟高[1,2,3]

[1]北京工业大学材料与制造学部激光工程研究院，北京 100124；

[2]北京工业大学跨尺度激光成型制造技术教育部重点实验室，北京 100124；

[3]北京市激光应用技术工程技术研究中心，北京 100124

摘要 钻孔是骨折修复手术中最常见的临床操作，骨孔的微观组织对骨折稳固及后期愈合具有显著影响。系统研究了激光钻切骨孔的微观组织特征和抗失稳行为，通过探究功率密度对激光钻切骨孔周围组织弹性模量的影响，结合分形方法对骨孔微观结构进行了量化分析与评价，并针对非均质骨微观结构，模拟分析对比了激光钻切骨孔与机械钻切骨孔在轴向力作用下的抗失稳行为。结果表明，在激光功率密度为 5.70×10^4 W/cm^2、扫描速度为 4 mm/s 的优化工艺参数下，骨孔边缘弹性模量受影响区宽度仅为 200 μm，较机械钻切骨孔缩小了 67%，壁面无裂纹，其余区域保持了骨组织的本征结构与力学特性。在轴向力作用下，激光钻切骨孔裂纹会在骨黏合线周围发生抑止或偏转，这有效提升了骨孔的抗失稳破坏能力，对增强内固定手术的稳定性有重要作用。

关键词 医用光学；激光技术；骨钻孔；微观组织；抗失稳行为

中图分类号 TN249 **文献标志码** A **DOI**: 10.3788/CJL230462

1 引 言

内固定术是治疗骨折的主要手段，手术中需要进行骨钻孔以提供骨通道，进而安装皮质骨螺钉[1]。皮质骨螺钉的内固定稳定性主要依靠螺钉与骨组织界面间的紧固力。在传统机械钻骨过程中，过大的切削力和扭矩极易损害骨孔的微观组织结构，产生裂纹与骨屑，从而严重影响骨孔的抗失稳破坏能力及愈后效果。Singh 等[2]进行了超声振动辅助钻头（RUBD）与普通外科钻头（CSBD）骨钻孔的对比研究，发现 RUBD 能够减小骨孔壁面的裂纹数量和尺寸，从而提高骨孔的抗失稳破坏能力。然而，RUBD 钻骨技术仍属于接触式的机械去除方式，通过转速和进给量的优化无法进一步提升骨孔的抗失稳性能。

激光钻切是一种非接触加工方式，具有更大的自由度和更高的精度，可以通过非接触式去除方式有效降低钻切区域组织的损伤并提高精度[3-5]。近几年随着医工交叉研究的深入推进，激光钻切在骨折治疗等外科手术中的潜在应用优势获得了越来越多的关注[6-9]。Matys 等[10]发现，与外科钻头和超声骨刀相比，激光骨钻切可以提高骨孔的精度（孔径和深度），有利于增强微型种植体与骨孔的接合强度。Panduric 等[11]在 Er:YAG 激光钻切骨孔组织的生物形态学研究中发现，激光钻切可以有效抑止骨孔壁面裂纹的扩展，而且激光钻切骨孔壁面更有利于细胞黏附和浸润，从而促进后期愈合。Robles-Linares 等[12-13]测试了机械钻切骨孔周围组织的弹性模量与抗压强度，仿真了皮质骨螺钉从机械钻切骨孔中拔出的全过程，获得了皮质骨螺钉拔出过程中骨孔的应力分布[14-15]。然而，该研究将骨组织简化为各向同性的刚体，并未考虑骨组织的非均质结构特征，不能真实展示骨孔的抗失稳行为。目前，激光钻切骨孔的研究还主要集中在宏观尺度的裂纹扩展行为方面[16]，关于骨孔微观组织特征和抗失稳行为的研究鲜有报道。激光钻切骨孔组织微观特征及其抗失稳行为的研究对于正确认识和推进面向临床手术的激光钻切技术具有重要意义。

本文针对激光钻切骨孔，系统分析了不同激光功率密度下骨孔周围组织弹性模量的分布特征，采用分形评价方法量化分析了激光钻切骨孔的微观组织特征，对激光钻切骨孔工艺进行优化，并在充分考虑骨的非均质结构特征的条件下探究了轴向力作用下骨孔的抗失稳行为。研究结果为激光钻切骨孔手术的临床应用提供了参考。

2 试验方法

羊的体重和代谢率与成年人相似[17]，因此，本文选

收稿日期：2023-01-16；**修回日期**：2023-02-15；**录用日期**：2023-02-16；**网络首发日期**：2023-03-09

基金项目：国家自然科学基金（51975017，52205437）、北京市教委科研重点项目（KZ202110005012）、北京市自然科学基金（3214041）

通信作者：*ncltji@bjut.edu.cn

取食品工业中的新鲜羊胫骨作为试验材料。试验前对离体生物骨样品进行标准处理[18]。骨组织中的水分对波长为 2 μm 的中红外激光有更高的吸收率[19]，吸收激光能量后水分在极短时间(<1 ms)内蒸发，在骨组织内部引起局部高压，产生“微爆”效应去除骨组织，有效降低热影响，因此本文采用波长为 2 μm 的中红外激光以旋切法在离体羊胫骨上钻切，获得直径为 3 mm 的通孔。在本试验条件下，当扫描速度≥4 mm/s，选择激光能量密度为 5.70×10^4、7.33×10^4、7.74×10^4、8.15×10^4、8.84×10^4、9.17×10^4 W/cm^{2}时，才能获得无热致碳化的骨通孔，因此选择最优激光参数范围进行对比研究。沿激光钻切骨孔样品中轴切开，分别用于分析骨孔的组织特征和测试骨孔周围组织的弹性模量。

骨孔的微观形貌采用扫描电子显微镜(SEM)进行观察分析。采用原子力显微镜(AFM)在大气和室温条件下测试钻切骨孔周围组织的弹性模量。测试区域自骨孔壁开始，径向总长度为 800 μm，如图 1 所示，将其分为四个区域：Ⅰ区(沿径向距离骨孔壁 0～200 μm)、Ⅱ区(沿径向距离骨孔壁 200～400 μm)、Ⅲ区(沿径向距离骨孔壁 400～600 μm)、Ⅳ区(沿径向距离骨孔壁 600～800 μm)。AFM 探针扫描区域尺寸为 40 μm×40 μm，测试扫描频率为每秒 1 次，分辨率为 512 pixel/line。

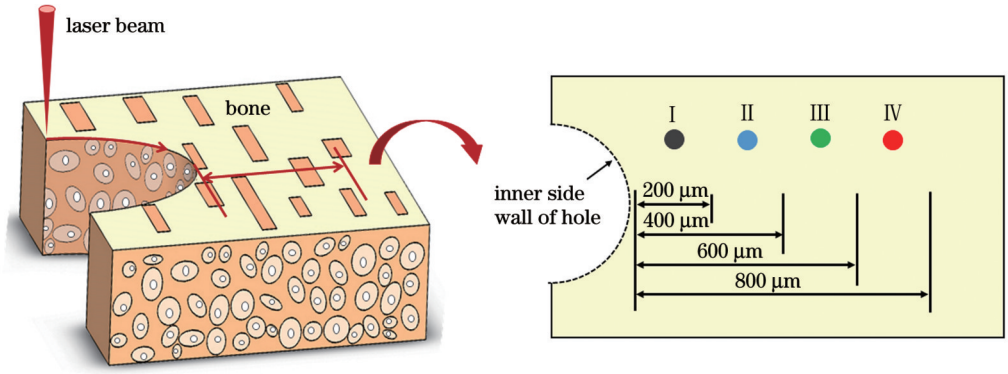

图 1 激光钻切骨孔周围组织的弹性模量测试位置示意图

Fig. 1 Schematic of elastic modulus test positions of tissues around bone hole drilled by laser

3 分析与讨论

不同功率密度激光钻切骨孔与机械钻切骨孔周围骨组织沿孔径向的弹性模量分布如图 2 所示。当激光功率密度大于等于 8.43×10^4 W/cm^{2}时，激光钻切骨孔周围骨组织的弹性模量分布特征与机械钻切骨孔一致，骨孔周围弹性模量受影响区域宽度均大于 600 μm，激光与机械钻切骨孔附近区域(Ⅰ、Ⅱ、Ⅲ区)骨组织

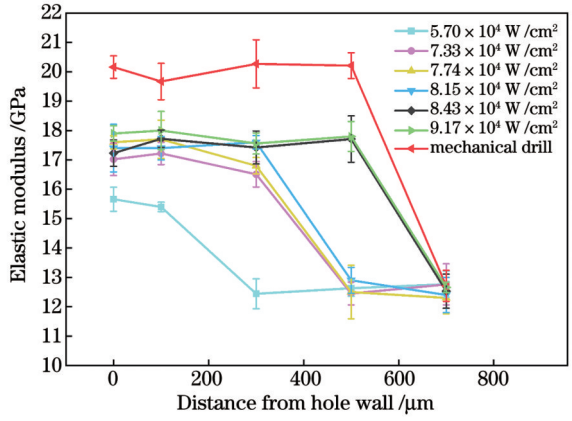

图 2 不同功率密度激光与机械钻切骨孔周围骨组织的弹性模量分布对比图

Fig. 2 Comparison of elastic modulus distributions of bone tissues around bone holes drilled by lasers with different power densities and by mechanical drill bit

的平均弹性模量分别为(17.7±0.5)GPa 和(20.1±0.6)GPa，与未钻切原始骨组织[(12.5±0.5)GPa]相比，分别增大了 41.6% 和 60.8%，仅距离骨孔壁最远的Ⅳ区保持了骨组织的本征结构。当激光功率密度下降到 7.33×10^4～8.15×10^4 W/cm^{2}时，激光钻切骨孔周围弹性模量受影响区域宽度缩小至 400 μm，激光钻切骨孔的力学特性优于机械钻切骨孔。当激光功率密度进一步降低为 5.70×10^4 W/cm^{2}时，激光钻切骨孔周围弹性模量受影响区域宽度进一步缩小，可以发现，激光钻切骨孔周围Ⅰ区测试的弹性模量为(15.5±0.3)GPa，略高于未钻切的原始骨组织；在距离骨孔壁 200～400 μm 的Ⅱ区，其骨组织的弹性模量为(12.6±0.4)GPa，与未钻切骨组织基本一致，基本保持了骨组织的本征结构。随着激光功率密度的降低，骨孔周围弹性模量受影响区域宽度逐渐减小，因此得到优化的激光功率密度为 5.70×10^4 W/cm^2，此时激光钻切骨孔周围弹性模量受影响区域的宽度为 200 μm，较机械钻切骨孔缩小了 67%。弹性模量是衡量骨组织力学特性的重要依据，弹性模量增大导致骨组织脆性增大，使得骨组织更易发生破坏[20]，激光钻切骨孔周围弹性模量受影响区域减小，表明激光技术最大程度降低了钻切对骨孔力学特性的影响，此时激光钻切骨孔的力学特性优于机械钻切骨孔。

激光钻切骨孔附近Ⅰ区是骨组织力学特性发生变

化的区域，通过对比Ⅰ区与Ⅱ区，进一步分析骨组织微观结构变化对其微观力学特性的影响。图 3(a1)、(a2)分别为原始骨组织的 AFM 形貌图和 DMT(Derjaguin-Muller-Toporov)模量分布图，DMT 模量图中较硬(弹性模量高)区域为骨组织中提供强度的矿物质颗粒，较软(弹性模量低)区域为骨组织中提供韧性的胶原纤维[图 3(a2)]，原始骨组织的胶原纤维按一定方向有序排列。当激光功率密度为 5.70×10^4 W/cm^{2}时，激光钻切骨孔附近Ⅰ区与Ⅱ区的 AFM 形貌分别如图 3(b1)和图 3(c1)所示，图 3(b2)和图 3(c2)分别为两个区域对应的 DMT 模量分布图。由图 3(b1)可知，在激光钻切过程中，骨孔附近Ⅰ区为最接近激光的区域，仅有部

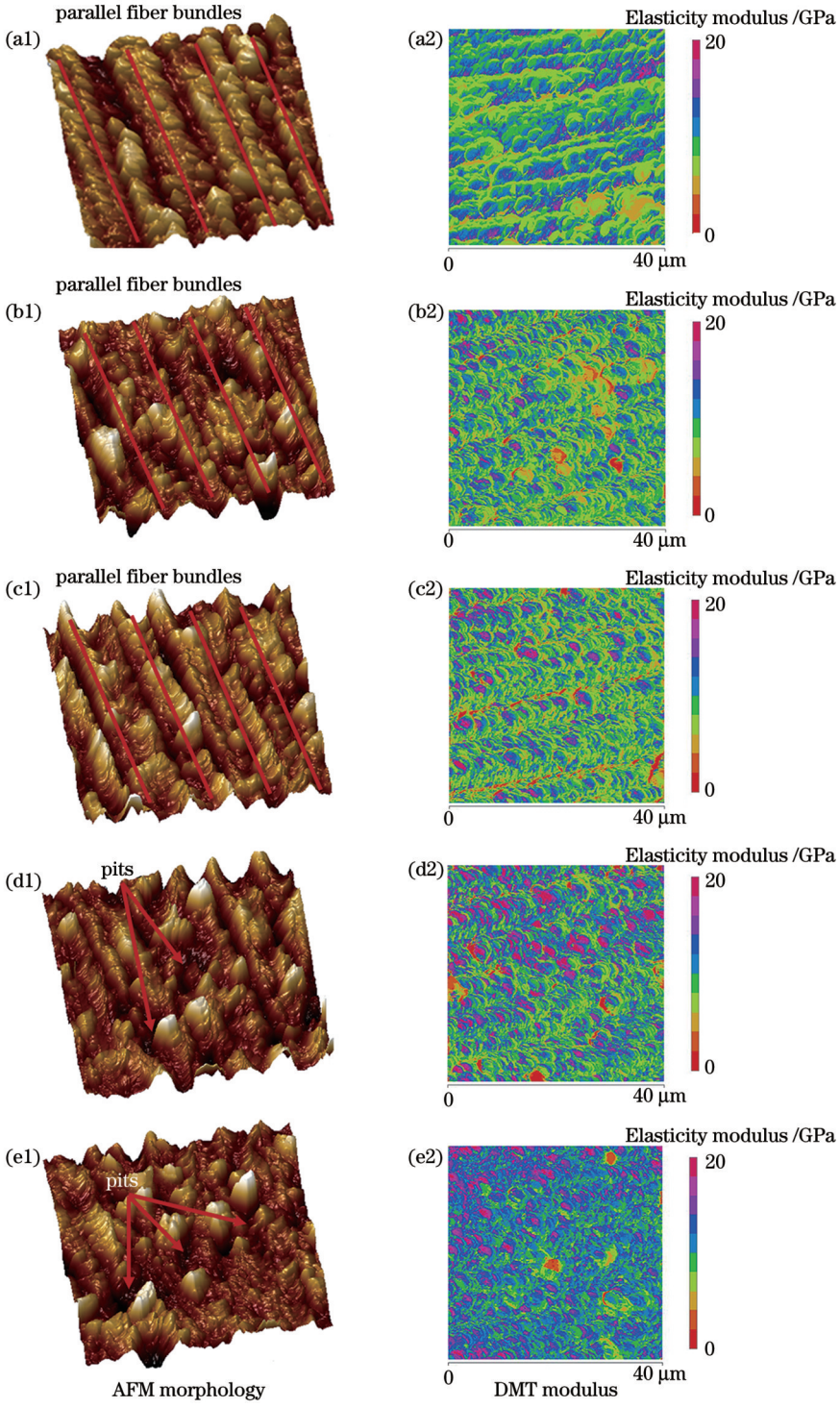

图 3　激光钻切与机械钻切骨孔周围骨组织的 AFM 形貌图和 DMT 模量图。(a1)(a2)原始骨组织；(b1)(b2)激光钻切骨孔附近Ⅰ区；(c1)(c2)激光钻切骨孔附近Ⅱ区；(d1)(d2)机械钻切骨孔附近Ⅰ区；(e1)(e2)机械钻切骨孔附近Ⅱ区

Fig. 3　AFM morphologies and DMT modulus diagrams of bone tissues around bone holes drilled by laser and by mechanical drill bit. (a1)(a2) Intrinsic bone tissue; (b1)(b2) region Ⅰ near bone hole drilled by laser; (c1)(c2) region Ⅱ near bone hole drilled by laser; (d1)(d2) region Ⅰ near bone hole drilled by mechanical drill bit; (e1)(e2) region Ⅱ near bone hole drilled by mechanical drill bit

分胶原纤维受热影响，个别矿物质颗粒呈团状分布在骨组织表面，仍可辨识出骨组织胶原纤维的排列方向[图 3(b2)]。骨孔附近Ⅱ区骨组织胶原纤维排列紧密，取向清晰[图 3(c1)]，矿物质颗粒均匀排列在胶原纤维表面[图 3(c2)]，保留了骨组织的本征结构。图 3(d1)和图 3(e1)分别为机械钻切骨孔附近Ⅰ区与Ⅱ区的AFM形貌图，机械钻切骨孔Ⅰ区与Ⅱ区的胶原纤维排列方向无法辨识，表明骨组织胶原纤维均发生了严重的热变形，导致该区域弹性模量增大，强度和韧性降低，并且大量矿物质颗粒呈团状分布，在骨组织表面形成多个孔隙，如DMT模量图中弹性模量为0的区域所示[图 3(d2)和图 3(e2)]，这些孔隙成为骨孔壁面的应力集中点，从而导致骨孔壁面失稳。由以上分析可知，激光钻切对骨孔周围组织的影响更小，对骨孔周围组织微观结构及弹性模量的影响更低，有利于提高骨孔的抗失稳能力。

基于分形理论的自相似原则，可以通过分数维数量化评价材料微观结构的不规则性和复杂性[21]，采用分形评价对骨孔周围Ⅰ区与Ⅱ区的骨组织微观结构进行表征，量化分析激光钻切骨孔组织微观结构的变化。AFM形貌图的负深度对应骨组织表面的孔隙，采用盒维数法从骨组织的AFM形貌图中提取相同深度，得到的黑色区域为孔隙面积。分形维数的盒维数[22]为

$$D=\lg N(\delta)/\lg\delta, \tag{1}$$

式中：D为分形维数；δ为以正方形网格边长为元素的递减序列；$N(\delta)$为覆盖目标所需的边长为δ的最小正方形网格数。以黑色区域面积与AFM图像总面积的比值为孔隙率，结果显示，激光钻切骨孔附近Ⅰ区与Ⅱ区骨组织表面的孔隙率均为0.17。根据式(1)计算得到激光钻切骨孔附近Ⅰ区与Ⅱ区的分形维数约为1.88，如图 4(a)、(b)所示，表明在优化后的激光功率密度5.70×10^4 W/cm^{2}下，激光钻切骨孔周围骨组织微观结构的变化很小，能基本保持骨组织的本征结构。而机械钻切骨孔附近Ⅰ区与Ⅱ区骨组织表面的孔隙率分别增大为0.26与0.23，分形维数分别增大为1.90与1.89[图 4(c)、(d)]。分形维数与孔隙率的增长表明钻切对骨组织微观结构的影响增大。机械钻切骨孔周围骨组织的分形维数和孔隙率较大，骨组织微观结构的无序性较明显，孔隙数量较多，表明机械钻切骨孔的组织受损较严重。

图 5(a)、(b)分别展示了激光钻切骨孔(激光功率密度为5.70×10^4 W/cm^2，扫描速度为4 mm/s)和机械钻切骨孔的SEM形貌。由图 5(a)可以看出，激光钻切骨孔壁面上开放的Haversian管清晰可见，未出现裂纹、熔凝、骨屑等组织损伤现象，愈合过程中骨组织内部的血液输运与细胞黏附得到促进，骨组织的愈合加速；而机械钻切骨孔壁面布满裂纹[图 5(b)]，裂纹的最大长度超过骨组织断裂的临界长度(300 μm)[23]，骨孔壁面因钻头的接触式机械作用，发生Haversian管堵塞，愈合延迟。

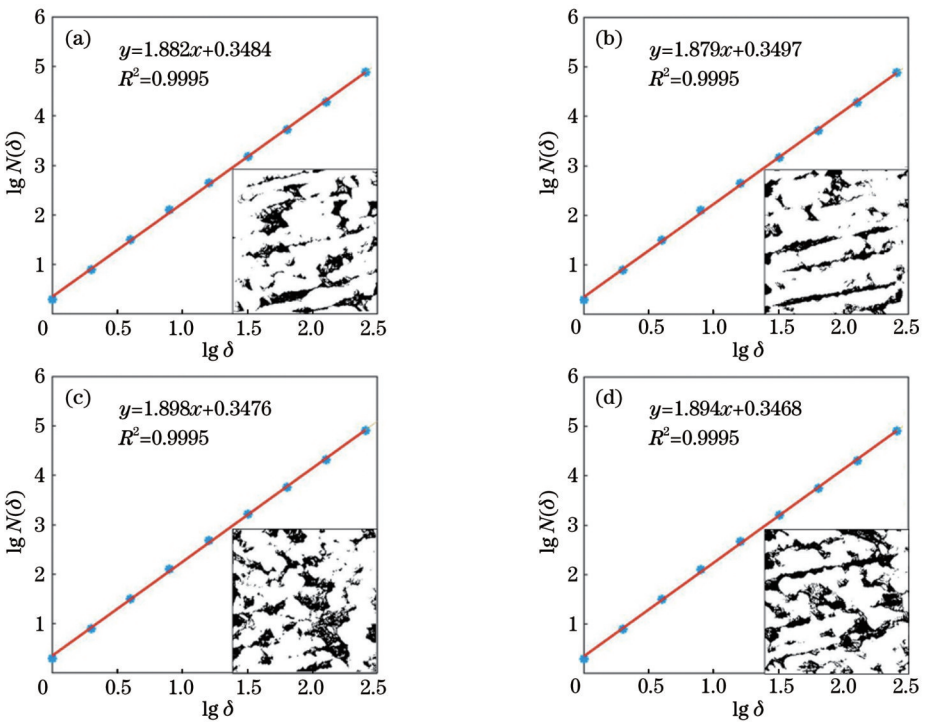

图4　基于AFM图像的骨组织分形特征分析。(a)激光钻切骨孔附近Ⅰ区；(b)激光钻切骨孔附近Ⅱ区；(c)机械钻切骨孔附近Ⅰ区；(d)机械钻切骨孔附近Ⅱ区

Fig. 4　Analysis of fractal characteristics of bone tissues based on AFM images. (a) Region Ⅰ near bone hole drilled by laser; (b) region Ⅱ near bone hole drilled by laser; (c) region Ⅰ near bone hole drilled by mechanical drill bit; (d) region Ⅱ near bone hole drilled by mechanical drill bit

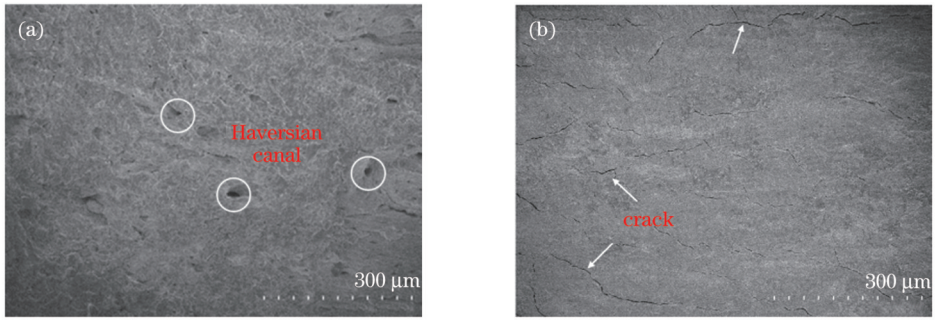

图 5　骨孔壁面的SEM形貌图。(a)激光钻切骨孔;(b)机械钻切骨孔

Fig. 5　SEM images of inner-wall of bone hole. (a) Bone hole drilled by laser; (b) bone hole drilled by mechanical drill bit

根据上述所测得的激光钻切骨孔力学参量,建立轴向拉力作用下皮质骨螺钉紧固于骨组织内部的力学模型,以分析激光钻切骨孔的抗失稳行为。考虑骨微观结构及其材料性能,建立一个由骨单位(osteon)、间质骨基质(interstitial matrix)、骨黏合线(cement line)和Haversian管组成的非均匀四相复合模型[24]。对内置在骨孔内的皮质骨螺钉加载轴向拉力,细化加载区域和骨组织的材料边界上的网格,模型尺寸为2 mm×5 mm,建立的有限元模型如图6(a)所示。在轴向拉力作用下,激光钻切与机械钻切骨孔的应力分布如图6(b)、(c)所示,可以看出,与机械钻切骨孔相比,激光钻切骨孔中骨组织的应力集中倾向显著降低。对于两种钻切方式,其应力均倾向于累积在间质骨基质中,但其裂纹萌生与扩展行为具有显著差异。在激光钻切骨孔中,裂纹遇到骨单位后无法穿透骨黏合线,而是在骨黏合线周围发生抑止或偏转,骨单位充分发挥了屏障作用[图6(b)]。而在机械钻切骨孔中,裂纹直接穿透骨黏合线进入骨单位,骨单位无法抑止裂纹的扩展,导致骨孔壁面失稳[图6(c)]。由此可知,当激光功率密度优化为5.70×10^4 W/cm^{2}时,有效减小了骨孔周围弹性模量的变化范围,骨单位起到屏障作用,裂纹遇到骨单位后在骨黏合线周围发生抑止或偏转,因此有效提升了骨孔的抗失稳破坏能力。

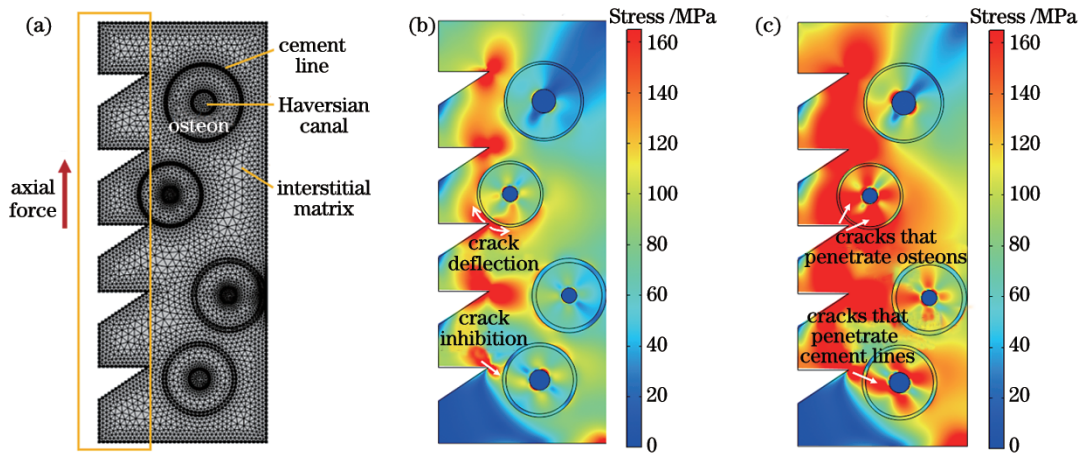

图 6　轴向力作用下骨孔壁面抗失稳过程的有限元模拟。(a)皮质骨螺钉内置于非均匀四相复合骨组织的有限元模型;(b)激光钻切骨孔应力分布;(c)机械钻切骨孔应力分布

Fig. 6　Finite element simulation of bone hole wall anti-instability under axial force. (a) Finite element model with cortical bone screw inserted in heterogeneous four-phase composite bone tissue; (b) stress distribution in hone hole drilled by laser; (c) stress distribution in bone hole drilled by mechanical drill bit

4　结　　论

通过试验与模拟相结合的方法,研究了激光钻切骨孔的微观组织特征与抗失稳行为。通过测试分析不同功率密度激光钻切后骨孔的微观结构和周围组织的弹性模量,并结合骨孔微观结构的分形量化评价,发现靠近激光作用区的骨组织分形维数和孔隙率分别为1.88和0.17,骨孔周围骨组织保持了微观结构的本征特征。确定优化的激光功率密度为5.70×10^4 W/cm^2,当扫描速度为4 mm/s时,所获骨孔壁面无裂纹,骨孔边缘弹性模量受影响区域宽度仅为200 μm,比机械钻切骨孔周围弹性模量受影响区域宽度缩小了67%。通过有限元分析对比了激光钻切与机械钻切骨孔在轴向力作用下壁面的应力分布,结果表明,激光钻切骨孔的应力集中倾向显著降低,裂纹沿骨黏合线发生抑止和偏转,骨单位充分起到了屏障作用,增强了激光钻切骨孔的抗失稳能力。研究结果为激光钻切骨的手术临床应用提供了参考。

参 考 文 献

[1] Tsai Y Y, Chang S W. Pullout strength of triply periodic minimal surface-structured bone implants[J]. International Journal of Mechanical Sciences, 2023, 237: 107795.

[2] Singh R P, Gupta V, Pandey P M, et al. Effect of drilling techniques on microcracks and pull-out strength of cortical screw fixed in human tibia: an *in-vitro* study[J]. Annals of Biomedical Engineering, 2021, 49(1): 382-393.

[3] 杨强, 季凌飞, 徐博, 等. 皮秒激光微制造 As_2Se_3 玻璃红外增透性表面[J]. 光电工程, 2017, 44(12): 1200-1209, 1247.
Yang Q, Ji L F, Xu B, et al. Picosecond laser microfabrication of infrared antireflective functional surface on As_2Se_3 glass[J]. Opto-Electronic Engineering, 2017, 44(12): 1200-1209, 1247.

[4] Han J, Liu Y, Deng Z J, et al. Optimizing noise characteristics of mode-locked Yb-doped fiber laser using gain-induced RIN-transfer dynamics[J]. High Power Laser Science and Engineering, 2021, 9: e36.

[5] Chen L, Liu Z L, Guo C, et al. Nanosecond laser-induced controllable periodical surface structures on silicon[J]. Chinese Optics Letters, 2022, 20(1): 013802.

[6] 赵海滨, 张先增, 詹振林, 等. 组织表面附着水膜层对脉冲 CO_2 激光骨硬组织消融的影响[J]. 中国激光, 2011, 38(1): 0104002.
Zhao H B, Zhang X Z, Zhan Z L, et al. Influence of an applied water film on bone hard tissue ablation with pulsed CO_2 laser[J]. Chinese Journal of Lasers, 2011, 38(1): 0104002.

[7] 张先增, 郭健, 詹振林, 等. 脉冲 CO_2 激光伴水喷雾的骨组织消融[J]. 光学学报, 2010, 30(7): 2069-2073.
Zhang X Z, Guo J, Zhan Z L, et al. Water spray-assisted ablation of bone hard tissue with pulsed CO_2 laser[J]. Acta Optica Sinica, 2010, 30(7): 2069-2073.

[8] Li C L, Fisher C J, Burke R, et al. Orthopedics-related applications of ultrafast laser and its recent advances[J]. Applied Sciences, 2022, 12(8): 3957.

[9] Song Y, Hu G Q, Zhang Z, et al. Real-time spectral response guided smart femtosecond laser bone drilling[J]. Optics and Lasers in Engineering, 2020, 128: 106017.

[10] Matys J, Flieger R, Tenore G, et al. Er: YAG laser, piezosurgery, and surgical drill for bone decortication during orthodontic mini-implant insertion: primary stability analysis: an animal study[J]. Lasers in Medical Science, 2018, 33(3): 489-495.

[11] Panduric D G, Juric I B, Music S, et al. Morphological and ultrastructural comparative analysis of bone tissue after Er: YAG laser and surgical drill osteotomy[J]. Photomedicine and Laser Surgery, 2014, 32(7): 401-408.

[12] Robles-Linares J A, Axinte D, Liao Z R, et al. Machining-induced thermal damage in cortical bone: Necrosis and micro-mechanical integrity[J]. Materials & Design, 2021, 197: 109215.

[13] Zhou Y X, Kastner M J, Tighe T B, et al. Elastic modulus mapping for bovine cortical bone from submillimeter- to submicron-scales using PeakForce Tapping atomic force microscopy[J]. Extreme Mechanics Letters, 2020, 41: 101031.

[14] Chatzistergos P E, Magnissalis E A, Kourkoulis S K. A parametric study of cylindrical pedicle screw design implications on the pullout performance using an experimentally validated finite-element model[J]. Medical Engineering & Physics, 2010, 32(2): 145-154.

[15] 严亚波, 裴国献, 桑宏勋, 等. 螺钉-骨抗拔出力试验有限元模型的建立与验证[J]. 中华创伤骨科杂志, 2013, 15(1): 28-31.
Yan Y B, Pei G X, Sang H X, et al. Screw-bone finite element models for screw pullout simulation[J]. Chinese Journal of Orthopaedic Trauma, 2013, 15(1): 28-31.

[16] Zhang J R, Guan K, Zhang Z, et al. *In vitro* evaluation of ultrafast laser drilling large-size holes on sheepshank bone[J]. Optics Express, 2020, 28(17): 25528-25544.

[17] McGovern J A, Griffin M, Hutmacher D W. Animal models for bone tissue engineering and modelling disease[J]. Disease Models & Mechanisms, 2018, 11(4): dmm033084.

[18] Ji L F, Zhang L T, Cao L J, et al. Laser rapid drilling of bone tissue in minimizing thermal injury and debris towards orthopedic surgery[J]. Materials & Design, 2022, 220: 110895.

[19] Parker S. Surgical lasers and hard dental tissue[J]. British Dental Journal, 2007, 202(8): 445-454.

[20] Chang Z, Chen P Y, Chuang Y J, et al. Zebrafish as a model to study bone maturation: Nanoscale structural and mechanical characterization of age-related changes in the zebrafish vertebral column[J]. Journal of the Mechanical Behavior of Biomedical Materials, 2018, 84: 54-63.

[21] 陈列, 文关棋, 郭飞, 等. 纳秒激光诱导超疏水硅橡胶表面微结构的分形特性[J]. 中国激光, 2021, 48(6): 0602201.
Chen L, Wen G Q, Guo F, et al. Fractal characteristics of microstructures on a superhydrophobic silicone rubber surface induced by a nanosecond laser[J]. Chinese Journal of Lasers, 2021, 48(6): 0602201.

[22] Kim G J, Yoo H S, Lee K J, et al. Image of the micro-computed tomography and atomic-force microscopy of bone in osteoporosis animal model[J]. Journal of Nanoscience and Nanotechnology, 2018, 18(10): 6726-6731.

[23] O'Brien F J, Taylor D, Clive Lee T. The effect of bone microstructure on the initiation and growth of microcracks[J]. Journal of Orthopaedic Research, 2005, 23(2): 475-480.

[24] Shu L M, Sugita N. Analysis of fracture, force, and temperature in orthogonal elliptical vibration-assisted bone cutting[J]. Journal of the Mechanical Behavior of Biomedical Materials, 2020, 103: 103599.

Microstructure and Anti-Instability Behavior of Bone Hole Drilled by Laser for Clinical Surgery

Chen Mengxue[1,2,3], Ji Lingfei[1,2,3*], Zhang Litian[1,2,3], Cao Lijie[1,2,3], Wei Hangru[1,2,3], Sun Weigao[1,2,3]

[1]*Institute of Laser Engineering, Faculty of Materials and Manufacturing, Beijing University of Technology, Beijing* 100124, *China*;

[2]*Key Laboratory of Trans-Scale Laser Manufacturing Technology of Ministry of Education, Beijing University of Technology, Beijing* 100124, *China*;

[3]*Beijing Engineering Research Center of Laser Applied Technology, Beijing* 100124, *China*

Abstract

Objective Bone drilling is the most common surgical intervention used to install implants and treat fractures, and the microstructure

of bone holes significantly affects fracture stability and the postoperative healing process. Traditional mechanical drilling can easily damage the microstructure of bone holes, produce cracks and bone chips, and seriously affect fracture stability. The contactless interaction of laser beams with bone has attracted increasing interest because it offers greater freedom and higher precision during drilling and provides a promising solution to improve the anti-instability performance of the drilled bone hole for clinical application. However, current studies on bone holes drilled by laser mainly focus on the analysis of macroscopic morphologies of bone cracks; moreover, the microstructure and anti-instability behavior of bone holes drilled by laser concerning heterogeneous structures are rarely investigated. To further promote the clinical application of the laser drilling of bone, this study systematically evaluates the microstructural characteristics and relationship between the microstructure and related anti-instability behavior of bone holes drilled by laser, which is helpful for optimizing the laser drilling strategy and providing guidance for the promotion of the laser drilling of bones for clinical application.

Methods Freshly extracted sheep tibia are selected for *in vitro* laser bone drilling. A mid-infrared laser with a wavelength of ~2 μm is used to drill 3 mm-diameter bone holes on the sheep tibia. First, the atomic force microscopy (AFM) is used to characterize and compare the elastic modulus distributions of the tissues around the bone holes drilled by a laser with different power densities and by a mechanical drill bit (Fig. 1). The microstructure of the bone-hole tissue is then quantitatively analyzed and evaluated using fractal evaluation. Subsequently, a heterogeneous four-phase composite model is established by considering the heterogeneous bone structure and mechanical properties of the bone hole. The stress distributions of the bone holes drilled by the laser and by mechanical drill bit under the action of axial force are simulated to visualize the anti-instability behavior of the drilled bone holes.

Results and Discussions The width of the elastic modulus affected zone around the bone hole decreases with decreasing laser power density (Fig. 2). Under the optimal laser power density of 5.70×10^4 W/cm^2 and scanning speed of 4 mm/s, the width of the elastic modulus affected zone near the bone hole edge is only 200 μm, the width of the elastic modulus affected zone of the hole bone drilled by laser is 67% smaller than that of the bone hole drilled by mechanical drill bit, and the other areas near the bone hole maintain the intrinsic microstructures and mechanical properties of the original bone tissues (Fig. 3). The fractal dimension analysis result shows that the fractal dimension and porosity of the bone tissue near the bone hole drilled by laser are 1.88 and 0.17, respectively, both of which are smaller than those of the mechanically drilled bone hole (Fig. 4). The results indicate that the microstructure of the bone tissue around the laser-drilled bone hole is hardly affected, the intrinsic structure of the bone tissue is maintained, and no cracks are observed on the bone hole wall (Fig. 5). The simulation results show that the stress concentration tendency of the laser-drilled bone hole is lower than that of a mechanically drilled bone hole under the action of axial force, and the cracks are inhibited or deflected around the cement line (Fig. 6), which effectively improve the instability resistance of the bone hole.

Conclusions In the present study, the microstructural characteristics and anti-instability behavior of laser-drilled bone holes are evaluated using the combination of experiments and simulations. It is found that the elastic modulus of the bone tissue around the bone hole tends to decrease with decreasing power density and increasing distance from the hole wall, and the effect of laser drilling on the elastic modulus distribution around the bone hole is relatively lower than that of mechanical drilling. A quantitative method for evaluating the microstructural morphology under laser action is established based on fractal evaluation, and the fractal dimension and porosity of bone tissue near the laser-drilled bone hole are merely 1.88 and 0.17, respectively, which are almost the same as the intrinsic structure parameters of bone tissue, indicating that laser drilling has a slight effect on the tissue around the bone hole, providing guidance for the optimization of laser drilling parameters. The optimized laser power density and scanning speed is 5.70×10^4 W/cm^2 and 4 mm/s, respectively, for minimal microstructural damage. The width of the elastic modulus affected zone around the bone hole is only 200 μm, which is 67% smaller than that of the mechanical-drilled bone. There are no cracks but open Haversian canals on the bone hole wall. The stress distribution is obtained using the finite element method to visualize the anti-instability behavior of the bone hole. The observed phenomenon reveals that the maximum stress propagates in the interstitial matrix; however, the growth of cracks caused by stress concentration is quite different for the laser- and mechanically-drilled bone holes. The cracks in the laser-drilled bone hole cannot penetrate the cement line, but are inhibited or deflected around the cement line, which improves the instability resistance of the bone hole. Our study shows that laser bone drilling is a new strategy for clinical applications that minimizes microstructural damage and improves fracture stabilization.

Key words medical optics; laser technique; bone drilling; microstructure; anti-instability behavior